Soft-core particles freezing to form a quasicrystal and a crystal-liquid phase

A. J. Archer,[1] A. M. Rucklidge,[2] and E. Knobloch[3]

[1]*Department of Mathematical Sciences, Loughborough University, Loughborough LE11 3TU, United Kingdom*
[2]*Department of Applied Mathematics, University of Leeds, Leeds LS2 9JT, United Kingdom*
[3]*Department of Physics, University of California, Berkeley, California 94720, USA*

Systems of soft-core particles interacting via a two-scale potential are studied. The potential is responsible for peaks in the structure factor of the liquid state at two different but comparable length scales and a similar bimodal structure is evident in the dispersion relation. Dynamical density functional theory in two dimensions is used to identify two unusual states of this system: a crystal-liquid state, in which the majority of the particles are located on lattice sites but a minority remains free and so behaves like a liquid, and a 12-fold quasicrystalline state. Both are present even for deeply quenched liquids and are found in a regime in which the liquid is unstable with respect to modulations on the smaller scale only. As a result, the system initially evolves towards a small-scale crystal state; this state is not a minimum of the free energy, however, and so the system subsequently attempts to reorganize to generate the lower-energy larger-scale crystals. This dynamical process generates a disordered state with quasicrystalline domains and takes place even when this large scale is linearly stable, i.e., it is a nonlinear process. With controlled initial conditions, a perfect quasicrystal can form. The results are corroborated using Brownian dynamics simulations.

I. INTRODUCTION

In hard condensed matter systems, the structure of the crystalline states that are formed is largely determined by the strength of the bonds between the atoms or molecules in the system, the dependence of the bonds on the orientation of the particles, and the packing of the particles. In general, thermal fluctuations and entropy are less important, unless one considers a system near the melting transition. In contrast, entropy and temperature can be all-important in determining the structure of soft-matter systems.

For polymers in solution, the interactions between pairs of chains depend on a delicate balance between energy and entropy [1]. When the solvent is good, the polymer chains form an open structure and interactions between pairs of polymers are largely repulsive and entropic in origin. On the other hand, when the solvent is not as good, the polymer exhibits a tendency to collapse. In a good solvent, the strength of the repulsion depends on how branched the polymer is. As a result, the form of the effective interaction between polymers can be tailored and controlled via the polymer architecture. In star polymers, for example, the effective interaction potential is determined by the number of arms on each star [1–3].

The effective interaction between soft polymeric macromolecules is also soft. Since the centers of mass need not coincide with any particular monomer, the effective interaction potential between the centers of mass can actually be finite for all values of the separation distance r between the centers. In this paper we discuss the structure, phase behavior, and dynamics of a two-dimensional (2D) model system of such soft-core particles.

The model that we study consists of soft particles that have a core plus corona (or shoulder) architecture. The particles interact via the following pair potential:

$$V(r) = \epsilon e^{-(r/R)^8} + \epsilon a e^{-(r/R_s)^8}, \qquad (1)$$

where R is the diameter of the cores of the particles and $R_s > R$ is the diameter of the corona (or shoulder) of the particles. In addition to the two length scales present in the potential, there are two energy scales: the energy penalty for a pair of particle cores to overlap is $\epsilon(1 + a)$ and the energy penalty for just the coronas to overlap is ϵa, where a is a dimensionless parameter that determines the shoulder repulsion strength.

The particular form of the pair potential in Eq. (1) arises from considering the effective interaction between the centers of mass of certain dendrimers or star polymers. For dendrimers, this potential applies if the inner generations of monomers are of one kind (hydrophobic, say), while the outer generations are of another kind (hydrophilic, say). Similarly, if a star polymer is made of diblock copolymers, then with a suitable choice of the block length ratio, the effective interaction potential between the centers of mass is expected to be of the form in Eq. (1) [4,5].

In Fig. 1, see Ref. [6], we display the phase diagram for a system with temperature $k_B T/\epsilon = 1$ and $R_s/R = 1.855$. The figure shows the $(a, \rho_0 R^2)$ plane, where $\rho_0 = \langle N \rangle / L^2$ and $\langle N \rangle$ is the average number of particles in area L^2. This phase diagram is determined using density functional theory (DFT). This theory, together with other results reported in [6], is elaborated below. We see that at low densities ρ_0 the particles form a liquid state. However, as the density increases, the particles overlap and then freeze to form one of two different crystalline states. The crystals are unusual: they are of the so-called cluster-crystal variety [5,7–13], related to the fact that the particles have a soft core. In the cluster-crystal multiple particles occupy each lattice site. When the parameter $a = 0$, the system reduces to particles interacting via a simple soft potential with one length scale and one energy scale. This is the generalized exponential model with exponent $n = 8$, or the GEM-8 model fluid [7–14]. In two dimensions, at the temperatures relevant here, this model exhibits just one hexagonal crystal phase, with lattice spacing $\sim R$ that is approximately constant with increasing density (note that
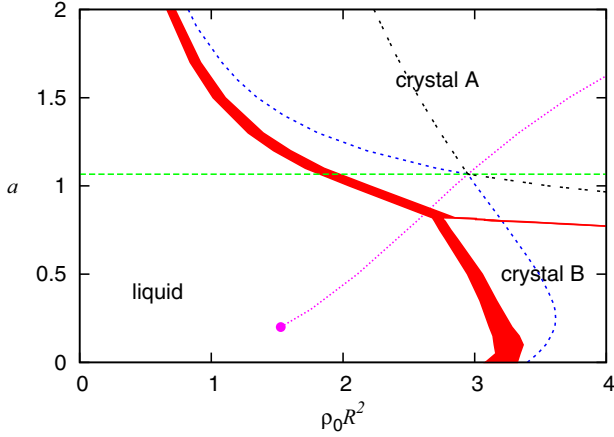
FIG. 1. (Color online) Phase diagram in the $(a, \rho_0 R^2)$ plane, where ρ_0 is the average density. The system exhibits three phases: a liquid and two crystalline phases. Crystal A is hexagonal, with a large lattice spacing, while crystal B, which is also hexagonal, has a smaller lattice spacing. The short-dashed blue line is the linear instability threshold (spinodal) for the uniform liquid. The long-dashed green horizontal line is where the two principal peaks in the static structure factor $S(k)$ have the same height, while the pink dotted line terminating in a circle is the locus where the two peaks in the dispersion relation $\omega(k)$ have equal height. The circle marks the point where the smaller k peak disappears.

at very low temperatures, a series of isostructural phase transitions is expected [12,13]). Similarly, when $a \gg 1$ the contribution from the core of the potential becomes negligible and the fluid is again approximately a GEM-8 system, but now the particles have the larger diameter R_s and a stronger repulsion energy. Thus, for large a, the system forms a hexagonal crystal with lattice spacing $\sim R_s$. We henceforth refer to this larger lattice spacing crystal as the crystal A phase and the smaller lattice spacing crystal as the crystal B phase.

When the difference $R_s - R$ is small, one can pass smoothly from one crystal phase to the other as a is varied (i.e., there is only one crystalline phase). However, when the difference is larger, as in the case displayed in Fig. 1, crystal A and crystal B are two distinct phases separated by a phase transition at $a \sim O(1)$.[1] Indeed, many of the interesting properties of the present model described below all occur in the regime where $a \sim O(1)$, because they stem from the competition between the two different length scales R and R_s and the two different energy scales $(1 + a)\epsilon$ and $a\epsilon$.

Two of the most striking properties of this system are that (i) when quenched to certain regions of the phase diagram, where $a \sim O(1)$, the system can sometimes freeze to form states with quasicrystalline order, and (ii) on examining in detail the crystal A phase, again when $a \sim O(1)$, we find that there is a high proportion of mobile particles in the system,

which is why we refer to this phase as a crystal-liquid state. It is crystalline, because the majority of the particles in the system is frozen onto a regular hexagonal lattice. However, a minority is liquid, in the sense that they move throughout the system. We find that the proportion of mobile particles in the system can be as high as 7%.

The quasicrystals (QCs) formed by the present system are a local equilibrium state of the system, i.e., they are not the global minimum free energy state. They are found at state points in the portion of the phase diagram where the thermodynamic equilibrium phase is the crystal-liquid A state. The QCs are formed by a particular dynamic mechanism when the system is quenched to certain regions of the phase diagram.

In order to find parameter values at which QCs might be favored, we have invoked understanding developed from analyzing mode interactions in the Faraday wave experiment, in which a tray of liquid is subjected to vertical vibrations of sufficient amplitude that standing waves form on the surface. This system exhibits quasipatterns (the fluid dynamical analog of quasicrystals), as discovered in the early 1990s [15,16], and two different mechanisms for their formation have been identified (see [17] for a more detailed discussion). Briefly, patterns with Q-fold symmetry are expressed as sums of modes with Q wave vectors spaced at equal angles and weakly nonlinear theory is used to compute how waves with different orientations affect each other. One mechanism relies on strong self-coupling to downplay the effect of waves with different orientations [18–20], so permitting 8-, 10-, 12-, 14-, 16-, 18-, 20-fold, or higher quasipatterns [17]. The second mechanism invokes nonlinear coupling between the primary waves with secondary weakly damped (or weakly excited) waves such that primary waves with wave vectors separated by a certain angle determined by the ratio of the primary to secondary wave number are favored [16,21–27]. We invoke here this second mechanism, as done in [28,29], and select the length scale ratio for our investigation to be $R_s/R = 1.855$ (Sec. III) in order that the ratio of the primary to secondary wave numbers is $2\cos(15°) = 1.932$, so favoring dodecagonal quasicrystals.

In fact, the mechanism for QC formation that we actually observe differs from either of the two mechanisms described above. The QCs form when the uniform liquid is linearly unstable against density fluctuations with a small wavelength that is close to that of the lattice spacing of the crystal B phase but stable with respect to wavelengths comparable to that of crystal A. Thus, in the initial stages after a quench the system appears to be forming the crystal B phase. However, the minimum free energy structure is actually the larger lattice spacing crystal A phase. In the subsequent *nonlinear* evolution, the system seeks to form this larger lattice-spacing phase. However, being already patterned with the shorter length scale from the early stage linear dynamics, the system cannot always form a perfect crystal A and often forms a state with a mixture of both the short and long length scales that sometimes turns out to have quasicrystalline ordering, i.e., the Fourier transform of the density distribution reveals the presence of 12-fold ordering. As one might expect from such a mechanism, the structure that is formed contains defects. However, by carefully controlling the wave numbers of the density modulations prior to the quench, the system can be induced to form a perfect quasicrystal.

---

[1]We estimate that crystal A and crystal B are distinct phases when $R_s/R \gtrsim 1.6$, since the ratio R_s/R needs to be greater than this value for there to be a point on the linear instability threshold line where there are two modes that are unstable (i.e., the point in Fig. 1 where the dotted and dashed lines meet).

Understanding the mechanisms by which soft-matter QCs can form is becoming increasingly important. The possibility of designing soft-matter quasicrystals that self-assemble has generated considerable interest at a fundamental level, leading to a burst of experimental and theoretical activity [30–34]. Self-assembled soft-matter quasicrystals are of interest for a number of reasons, not least because they promise to provide a route to manufacturing materials and coatings with novel optical or electronic properties arising as a consequence of their high degree of rotation symmetry [35–37].

Although our focus is on polymeric soft-matter QCs, we should also mention that there are other (colloidal) soft-matter systems that form QCs [34,38–42]. These also have pair potentials involving more than one length scale, but owing to the particles having a hard core, the local structure of these materials differs from that described below, as does the resulting phase behavior.

This paper is structured as follows. In Sec. II we describe the DFT and dynamical DFT that we use to determine the structures formed by the system. In Sec. III we discuss the properties of the uniform liquid state, presenting results for the radial distribution function $g(r)$, the static structure factor $S(k)$, and the dispersion relation $\omega(k)$. We then present results relating to the solid states that are formed, focusing on the crystal-liquid state in Sec. IV and on QC formation in Sec. V. This section includes a discussion of our numerical results and their relation to other mechanisms of QC formation from the literature that are relevant to soft-matter systems. The paper concludes in Sec. VI with a few concluding remarks.

II. THEORY FOR THE SYSTEM

We use DFT [43–46] to determine the structure, thermo-dynamics, and phase behavior of the system. To describe the dynamics of the system when it is out of equilibrium, we use dynamical density functional theory (DDFT) [47–50]. The thermodynamic grand potential of the system is a functional of the one-body density distribution $\rho(\mathbf{r})$ of the particles

$$\Omega[\rho(\mathbf{r})] = F[\rho(\mathbf{r})] + \int d\mathbf{r}\rho(\mathbf{r})[\Phi(\mathbf{r}) - \mu], \quad (2)$$

where μ is the chemical potential, $\Phi(\mathbf{r})$ is the external potential, and $F[\rho]$ is the intrinsic Helmholtz free energy of the system, which is composed of two contributions

$$F[\rho(\mathbf{r})] = k_B T \int d\mathbf{r}\rho(\mathbf{r})[\ln(\rho(\mathbf{r})\Lambda^2) - 1] + F_{\text{ex}}[\rho(\mathbf{r})]. \quad (3)$$

The first term is the ideal-gas contribution, with k_B the Boltzmann constant, T the temperature, and Λ the thermal de Broglie wavelength. The second term F_{ex} is the excess (beyond ideal gas) portion describing the contribution to the free energy stemming from the interactions among the particles. The equilibrium density profile of the system at a given state point (μ, T) is that which minimizes $\Omega[\rho]$, i.e., which satisfies the equation

$$\frac{\delta\Omega[\rho(\mathbf{r})]}{\delta\rho(\mathbf{r})} = 0. \quad (4)$$

For systems of soft-core particles such as those we consider here, the following rather simple mean-field approximation is

remarkably accurate [1,51,52]:

$$F_{\text{ex}}[\rho(\mathbf{r})] = \frac{1}{2} \int d\mathbf{r} \int d\mathbf{r}'\rho(\mathbf{r})V(|\mathbf{r} - \mathbf{r}'|)\rho(\mathbf{r}'). \quad (5)$$

This functional generates the following simple random-phase approximation (RPA) for the pair direct correlation function:

$$c^{(2)}(|\mathbf{r} - \mathbf{r}'|) \equiv -\beta\frac{\delta^2 F_{\text{ex}}[\rho(\mathbf{r})]}{\delta\rho(\mathbf{r})\delta\rho(\mathbf{r}')} = -\beta V(|\mathbf{r} - \mathbf{r}'|), \quad (6)$$

where $\beta = (k_B T)^{-1}$.

To calculate the density profile of the system at a given state point (μ, T), we discretize the density profile on a square Cartesian grid and use fast Fourier transforms to evaluate the convolution integrals in $F_{\text{ex}}[\rho]$. We employ standard Picard iteration [53] to solve the Euler-Lagrange equation obtained from Eqs. (2)–(4),

$$\ln[\rho(\mathbf{r})\Lambda^2] - c^{(1)}(\mathbf{r}) + \beta\Phi(\mathbf{r}) - \beta\mu = 0, \quad (7)$$

where

$$c^{(1)}(\mathbf{r}) \equiv -\beta\frac{\delta F_{\text{ex}}[\rho(\mathbf{r})]}{\delta\rho(\mathbf{r})} \quad (8)$$

is the one-body direct correlation function. For the RPA functional in Eq. (5) this gives

$$c^{(1)}(\mathbf{r}) = -\int d\mathbf{r}'\beta V(|\mathbf{r} - \mathbf{r}'|)\rho(\mathbf{r}'). \quad (9)$$

Equation (7) can be rearranged to obtain the following expression for the density profile:

$$\rho(\mathbf{r}) = \rho_0 \exp\{-\beta\Phi(\mathbf{r}) + c^{(1)}(\mathbf{r}) - c^{(1)}[\rho_0]\}, \quad (10)$$

where $c^{(1)}[\rho_0]$ denotes the value of $c^{(1)}$ when Eq. (9) is evaluated for the uniform density profile $\rho(\mathbf{r}) = \rho_0$. We note the result $\rho_0 = \Lambda^{-2}\exp(\beta\mu + c^{(1)}[\rho_0])$ showing that the average density in the system ρ_0 is determined by the chemical potential μ or vice versa.

Picard iteration of Eq. (10) corresponds to substituting the density profile at step j, $\rho^{(j)}(\mathbf{r})$, into the right-hand side of Eq. (10) to obtain $\rho_{\text{rhs}}^{(j)}(\mathbf{r})$. To stabilize the iteration process these two density profiles at step j are mixed,

$$\rho^{(j+1)}(\mathbf{r}) = \alpha\rho_{\text{rhs}}^{(j)}(\mathbf{r}) + (1 - \alpha)\rho^{(j)}(\mathbf{r}), \quad (11)$$

to obtain a new approximation for the density at step $j + 1$. This equation is then iterated until convergence is achieved. The value of the mixing parameter α varies, depending on the state point and the type of density profile to be calculated, but typically is in the range $0.001 < \alpha \lesssim 0.1$.

In the present study we generate the initial guess for the density profile in several different ways. One choice is to use the density profile obtained from solving at a different state point. Another way is to start with the density profile $\rho(\mathbf{r}) = \rho_0 + \xi(\mathbf{r})$, where $\xi(\mathbf{r})$ is a small amplitude randomly fluctuating field. When the uniform fluid is linearly unstable (see below in Sec. II C), this initial guess may converge to the density profile of the crystal. However, this method often results in density profiles containing defects. The chance of these forming is much less in smaller systems and so the density profile for a larger portion of a perfect crystal needs to be built up from the density profile obtained from a smaller system.

With this procedure the average density in the system

$$\bar{\rho} = \frac{1}{L^2} \int d\mathbf{r} \rho(\mathbf{r}) \qquad (12)$$

equals ρ_0 only when the system is in the uniform liquid state. For the crystal, $\bar{\rho} \neq \rho_0$. This is because by iterating (10), we actually select the value of the chemical potential μ. The density ρ_0 is the density of the uniform liquid for this value of μ and $\bar{\rho}$ is therefore the density of the crystal corresponding to this μ value. In calculations where we wish to specify the average density to be ρ_0, we add an additional step to the Picard iteration, where at each step j, after the mixing step given by Eq. (11), we renormalize the density profile, whereby we replace $\rho^{(j+1)}(\mathbf{r})$ with $f\rho^{(j+1)}(\mathbf{r})$, where $f = \rho_0/[\frac{1}{L^2} \int d\mathbf{r} \rho^{(j+1)}(\mathbf{r})]$ [cf. Eq. (12)]. In all our discussions below, we do not distinguish between $\bar{\rho}$ and ρ_0. We use ρ_0 to denote the average density in all phases, but it should be borne in mind that when this refers to a crystal phase, we mean the average density as defined in Eq. (12).

As presented, Picard iteration is simply a numerical algorithm for solving the Euler-Lagrange equation and therefore for finding density profiles that minimize the free energy. However, as shown in Sec. V, Picard iteration generates a series of density profiles that are often a fairly good approximation to the real dynamics as determined by DDFT (see Sec. II B), i.e., the index j can be thought of as if it were proportional to the time t. In these cases we have used the fictitious dynamics generated by Picard iteration in place of the slower DDFT to survey the behavior at different points in the phase diagram.

In Fig. 2 we display typical density profiles obtained from DFT when the temperature $k_B T/\epsilon = 1$ and $R_s/R = 1.855$. The phase diagram for this system is displayed in Fig. 1. In the top panel of Fig. 2 we display the density profile at an interface between coexisting crystal A and crystal B phases, for $a = 0.75$. Since the lattice spacings of the two crystal structures are incommensurate, defects are necessarily present along the interface. In the bottom panel of Fig. 2 we display the density profile across an interface between the uniform density liquid on the right and the small lattice spacing crystal B phase on the left, for $a = 0.5$.

In the phase diagram displayed in Fig. 1 the shaded (red) regions indicate coexistence between two different phases. The boundaries of these regions correspond to the densities of the two phases at coexistence; recall that for two phases to coexist the chemical potential μ, the pressure $p \equiv -\Omega/L^2$, and the temperature T must be equal in the two phases. There is also a triple point, where all three phases coexist. Note that in order to determine the minimum grand potential Ω one must also minimize with respect to the computational domain size L. Actually, for hexagonal crystals one should calculate the density on a domain of size $\sqrt{3}L \times L$. However, on comparing results on such domains with those obtained on a square domain, we have confirmed that as long as the (square) domain is sufficiently large that it contains many unit cells, the slight strain energy contribution to the free energy is negligible. Most of the calculations presented here are for a system of size $L = 25.6R$ with periodic boundary conditions, where the finite-size effects for the regular crystal structures are negligible. For QC structures, there are particular domain sizes (e.g., 8, 30, and 112 times the smaller scale) that allow
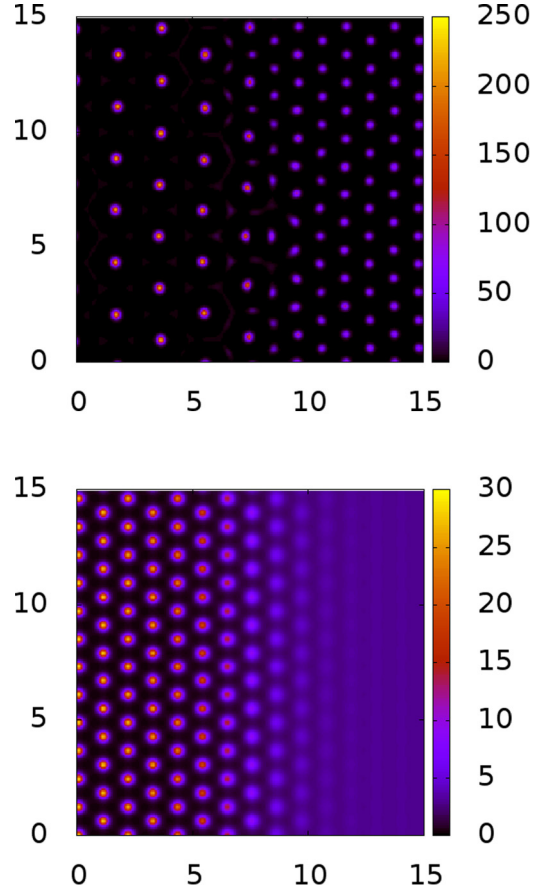

FIG. 2. (Color online) The top panel shows the density profile in the $(x/R, y/R)$ plane near an interface between coexisting crystal A and crystal B phases, for $a = 0.75$. Because the lattice spacings of the two crystal structures are not commensurate, defects along the interface are necessarily present. The bottom panel shows the density profile between the uniform liquid and the [1,1] interface of the crystal B phase, for $a = 0.5$.

for accurate approximation to 12-fold QC structure [17]. Our results are for domains of size 30. We remark further on this point in Sec. V.

A. Liquid structure factor

To characterize the structure of the liquid state, two quantities, the real space radial distribution function $g(r)$ and the reciprocal space static structure factor $S(k)$, are very useful [46]. The static structure factor in the liquid phase is given by the relation $S(k) = [1 - \rho_0 \hat{c}(k)]^{-1}$, where $\hat{c}(k)$ is the Fourier transform of $c^{(2)}(r)$. Thus the RPA for the structure factor in the uniform liquid phase is

$$S(k) = \frac{1}{1 + \rho_0 \beta \hat{V}(k)}. \qquad (13)$$

To determine the radial distribution function $g(r)$ one can insert the simple RPA (6) into the Ornstein-Zernike equation [46]. However, we choose instead to calculate $g(r)$ using the Percus test particle method [46,54]. This gives a more accurate approximation for $g(r)$ and also illustrates better the true accuracy of the DFT that we use. The test particle method

corresponds to fixing one of the particles at the origin, so that $\Phi(\mathbf{r}) = V(r)$ in Eq. (2), and then calculating the density distribution of the remaining particles in the presence of this fixed particle. The radial distribution function is obtained from the resulting density profile via Eq. (4): $g(r) = \rho(r)/\rho_0$. In Ref. [54] results from this RPA test particle theory were compared with the more sophisticated hypernetted-chain (HNC) theory for a very similar 2D soft-core system. The agreement between the two is rather good, which gives us confidence that the simple RPA DFT is accurate. We present typical results for $g(r)$ and $S(k)$ in Sec. III below.

B. Dynamics: Time evolution of the density

In addition to the equilibrium fluid structure, we also determine the nonequilibrium fluid dynamics. Since we consider soft polymeric blobs in solution, an appropriate approximation is to assume that the centers of mass of the particles move via Brownian motion, i.e., via overdamped stochastic equations of motion

$$\dot{\mathbf{r}}_i = -\Gamma\nabla U(\mathbf{r}^N,t) + \Gamma\mathbf{X}(t), \tag{14}$$

where $i = 1,\ldots,N$ is an index that labels all the different particles in the system, whose set of position coordinates we denote by $\mathbf{r}^N \equiv \{\mathbf{r}_1,\mathbf{r}_2,\ldots,\mathbf{r}_N\}$. The mobility coefficient $\Gamma = \beta D$, where D is the diffusion coefficient, while $\mathbf{X}(t)$ denotes the random force on the particles due to the solvent thermal motion. We assume in the standard way that $\mathbf{X}(t)$ is a Gaussian random variable [47–50]. The potential energy of the system is

$$U(\mathbf{r}^N,t) = \sum_{i=1}^{N}\Phi(\mathbf{r}_i) + \sum_{j>i}^{N}\sum_{i=1}^{N}V(|\mathbf{r}_i - \mathbf{r}_j|). \tag{15}$$

For a system of interacting particles with equations of motion given by (14), we can use DDFT [47–50] to determine the time evolution of the fluid nonequilibrium density distribution $\rho(\mathbf{r},t)$. In DDFT the dynamics is governed by

$$\frac{\partial\rho(\mathbf{r},t)}{\partial t} = \Gamma\nabla\cdot\left[\rho(\mathbf{r},t)\nabla\frac{\delta\Omega[\rho(\mathbf{r},t)]}{\delta\rho(\mathbf{r},t)}\right], \tag{16}$$

a result that follows on making the approximation that the nonequilibrium fluid two-point density correlation function is the same as that in the equilibrium fluid with the same one-body density distribution. Equation (16) is thus an approximation [47–50], but for soft-core fluids, previous good agreement with the results from Brownian dynamics (BD) computer simulations [i.e., from solving repeatedly Eq. (14) and then averaging over the different realizations of the noise] gives us confidence that Eq. (16) provides a good approximation to the exact dynamics.

C. Dispersion relation

An important quantity for understanding the behavior of the system is the dispersion relation $\omega(k)$. This relation determines the rate at which density fluctuations in the uniform liquid grow ($\omega > 0$) or decay ($\omega < 0$) over time. Consider a uniform liquid with density ρ_0, with a superposed small amplitude perturbation $\tilde{\rho}(\mathbf{r},t) \equiv \rho(\mathbf{r},t) - \rho_0$. Equation (16) shows that

the perturbation evolves according to

$$\frac{\partial\tilde{\rho}}{\partial t} = \mathcal{L}\tilde{\rho} + O(\tilde{\rho}^2), \tag{17}$$

where $\mathcal{L} \equiv D\nabla^2 - D\rho_0\nabla^2 c^{(2)}\otimes$ is a linear operator and $\otimes$ denotes a convolution, i.e., $c^{(2)}\otimes\tilde{\rho} \equiv \int d\mathbf{r}'c^{(2)}(\mathbf{r} - \mathbf{r}')\tilde{\rho}(\mathbf{r}')$. To obtain this result one must make a functional Taylor expansion of $F_{\mathrm{ex}}[\rho]$ [49,54,55]. Linearizing Eq. (17) and decomposing $\tilde{\rho}$ into a sum of different Fourier modes,

$$\tilde{\rho}(\mathbf{r},t) = \sum_{\mathbf{k}}\hat{\rho}_{\mathbf{k}}e^{i\mathbf{k}\cdot\mathbf{r}+\omega(k)t}, \quad k \equiv |\mathbf{k}|, \tag{18}$$

leads to the dispersion relation [49,54,55]

$$\omega(k) = -Dk^2[1 - \rho_0\hat{c}(k)]. \tag{19}$$

On combining this result with the RPA (6) we obtain $\omega(k) = -Dk^2[1 + \rho_0\beta\hat{V}(k)]$, a result closely connected to the structure factor $S(k)$ defined in Eq. (13). This connection applies in the case of a stable uniform liquid.

The liquid state is described as being linearly stable if $\omega(k) < 0$ for all wave numbers k and linearly unstable when $\omega(k) > 0$ for some wave number k. The latter situation arises for state points deep inside the parameter regime where the crystal is the equilibrium phase. The linear instability threshold is defined as the locus in the phase diagram where $\frac{d\omega(k)}{dk}|_{k=k_c} = 0$ together with $\omega(k = k_c) = 0$, i.e., the locus where the maximum growth rate is zero. The location of this threshold is displayed in Fig. 1 as the blue short-dashed line.

III. STRUCTURE OF THE LIQUID

In this section we present some typical results for the radial distribution function $g(r)$, the static structure factor $S(k)$, and the dispersion relation $\omega(k)$ to illustrate the changes in the structure of the uniform liquid as the average density ρ_0 and the shoulder height parameter a are varied.

In Fig. 3 we display a series of results for fixed $a = 0.8$, as the density of the fluid is increased from zero to the value $\rho_0 R^2 = 2.7$, which for $a = 0.8$ is the density of the liquid at coexistence with the crystal B phase. In the top panel we display the radial distribution function. In the limit $\rho_0 \to 0$ this is given by $g(r) = \exp[-\beta V(r)]$, which exhibits a correlation hole for small r due the particles seeking to avoid overlaps. However, since the repulsion strength for full overlap at this temperature is $\beta V(r = 0) = \beta\epsilon(1 + a) = 1.8$, which is not that large, $g(r \approx 0)$ is positive, reflecting the fact that there is a nonzero probability for particles to overlap completely, even at low densities. As the density ρ_0 increases, the value of $g(r \approx 0)$ also increases, reflecting the fact that particles are forced to overlap more often. Furthermore, oscillations develop in the tail of $g(r)$, at larger r. For particles with a hard core, we would normally ascribe this behavior to packing effects due to core exclusion. However, in the present system this is a largely energetic effect: as the density is increased, the overall energy is lowered if some particles overlap with each other completely, thereby avoiding more expensive partial overlap with many particles simultaneously, although the degree to which this occurs depends on the balance between energetic and entropic effects. This behavior is also reflected in the
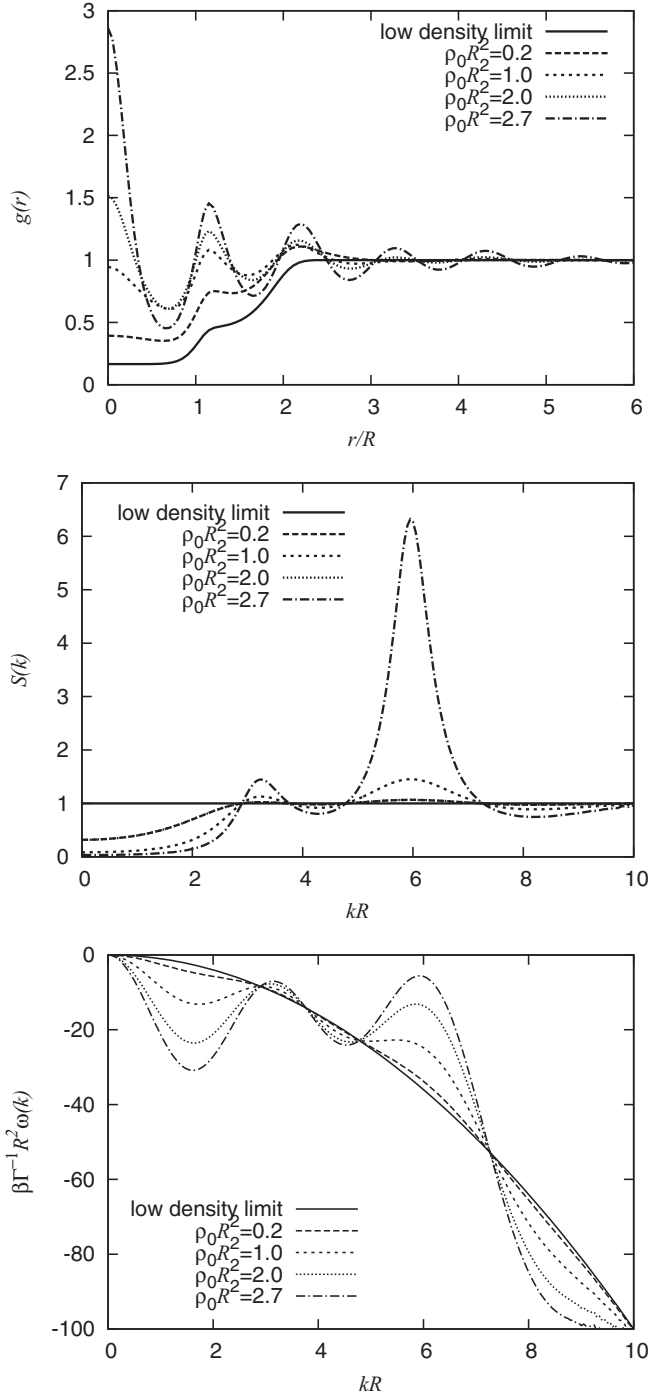
FIG. 3. Correlation functions characterizing the liquid phase for increasing density ρ_0 as indicated in the key, for fixed $a = 0.8$. The top panel shows the radial distribution function $g(r)$, the middle panel the static structure factor $S(k)$, and the bottom panel the dispersion relation $\omega(k)$.

fact that for $\rho_0 R^2 > 1$, $g(r \approx 0) > 1$. This value of $g(r \approx 0)$ continues to increase as the density is increased. For the case $\rho_0 R^2 = 2.7$ we see that $g(r)$ is highly structured, with a pronounced peak at $r = 0$ indicating multiple overlaps. In fact, it is this growing tendency to form clusters that drives freezing into a cluster crystal when the density $\rho_0 R^2 \gtrsim 2.7$.

In the middle panel of Fig. 3 we display the structure factor $S(k)$ obtained via Eq. (13) at the same density values. We see that as the density is increased, $S(k)$ exhibits two peaks. These reflect the correlations in the system with two characteristic length scales R and R_s and so the two peaks in $S(k)$ are (roughly) at the wave numbers $\approx 2\pi/R_s$ and $\approx 2\pi/R$. The fact that the peak at $\approx 2\pi/R$ is larger reflects the fact that for this value of a the particle core repulsions dominate the repulsions due to the shoulder. As a result, for this value of a ($a = 0.8$) the system freezes to form the small lattice spacing crystal B phase.

In the lower panel of Fig. 3 we display the dispersion relation $\omega(k)$ at the same series of state points. Except for the limiting case of low density, $\omega(k)$ also exhibits two peaks, reflecting the peaks in $S(k)$. For all the results displayed $\omega(k) \leqslant 0$ for all k from which we infer that the liquid is in fact linearly stable at these densities. Indeed, at these densities the uniform liquid is the global minimum free energy state. However, for $\rho_0 R^2 \gtrsim 2.7$, the global minimum corresponds to that of the hexagonal crystal. As the density is further increased (not displayed), the larger k peak in $\omega(k)$ continues to grow in height and when $\rho_0 R^2 \approx 3.2$ the peak growth rate $\omega(k = k_c) = 0$, indicating that the uniform liquid is now marginally unstable with respect to perturbations with wave number $k_c \approx 2\pi/R$. The resulting linear instability threshold (spinodal) line is displayed as the blue short-dashed line in Fig. 1.

In Fig. 4 we display $g(r)$ (top), $S(k)$ (middle), and $\omega(k)$ (bottom) at fixed density $\rho_0 R^2 = 1.2$, as the shoulder height parameter a is varied. For small values of a, we see that $g(r)$ exhibits a peak just beyond $r = R$, since this is the effective diameter of the particles. However, as a increases, increasing the shoulder height, this peak decreases in height while another peak develops just beyond $r = R_s$, reflecting the growing dominance of the shoulder in determining the correlations in the liquid. The liquid with density $\rho_0 R^2 = 1.2$ and $a = 1.3$ is at phase coexistence with the crystal A phase. The behavior observed in $g(r)$ is of course reflected in the structure factor shown in the middle panel of Fig. 4. Specifically, for small a there is a single peak in $S(k)$, at $kR \approx 5.5$. As the shoulder height a increases, this peak moves slightly towards larger k and a second peak develops at $kR \approx 3$, i.e., at a value of k that is a little below the value $2\pi/R_s$. The latter reflects the growing importance of the length scale R_s in the particle correlations in the liquid. As a increases further the peak at smaller k overtakes the larger k peak. The two peaks in $S(k)$ have equal height at $a = 1.067$, irrespective of the fluid density. The locus of this point is displayed as the green long-dashed line in Fig. 1. The lower panel of Fig. 4, which displays the dispersion relation $\omega(k)$, also shows the development and growth of a peak at $kR \approx 3$. Increasing a beyond the values displayed in this figure shows that this peak continues to grow in height until $\omega(k) > 0$ for $kR \approx 3$, indicating the uniform fluid becomes linearly unstable. In Fig. 1 we display the locus along which the two principal peaks in $\omega(k)$ are of equal height using a pink dotted line. Along this line the growth (or decay) rates for density fluctuations with these two wave numbers are the same.

In Fig. 5 we display the dispersion relation $\omega(k)$ for fixed $\rho_0 R^2 = 3.5$ and various values of a. For the case $a = 0.4$ there
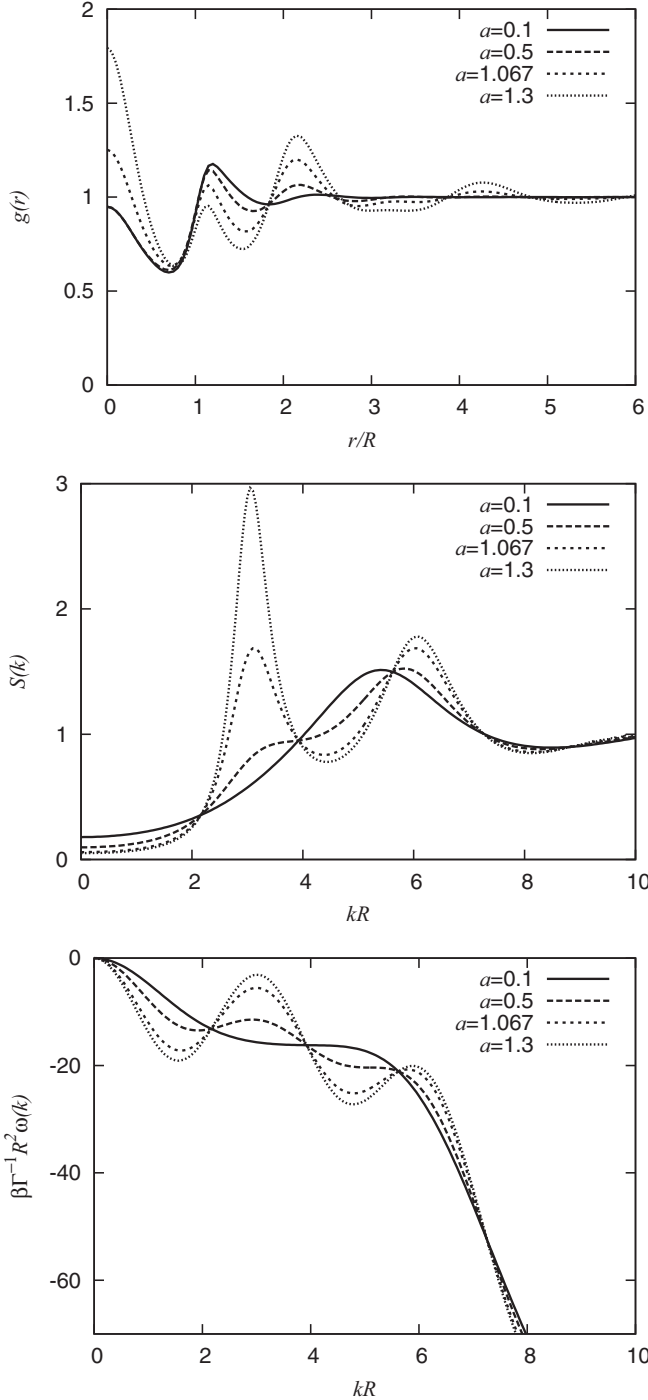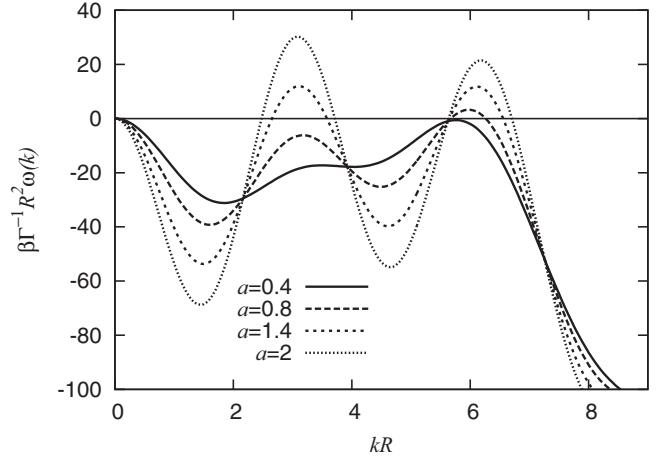
FIG. 5. Dispersion relation $\omega(k)$ for fixed $\rho_0 R^2 = 3.5$ and various values of a, as indicated in the key.

the dominant peak for $a > 1.4$. Since $\omega(k)$ determines the growth rate of density fluctuations in the unstable liquid, the figure reveals a transition between the fastest growing modes at small a to those at large a; this transition takes place along the pink dotted line in Fig. 1.

This can also be seen in Fig. 6, which displays the dispersion relation along a diagonal path in the phase diagram passing through the point $(\rho_0 R^2, a) = (2.95, 1.067)$, corresponding to the cusp in the blue short-dashed marginal stability threshold line in Fig. 1. At this point two modes with wave number ratio $k_2/k_1 = 1.932$ are marginally unstable.

IV. CRYSTAL-LIQUID STATE

We now turn our attention to the density profiles in the crystal state. As illustrated in Fig. 2, at first sight the crystal A and crystal B phases appear to be standard examples of hexagonally ordered cluster crystals. However, closer

FIG. 4. Correlation functions characterizing the liquid phase for a range of values of a as indicated in the key, for fixed $\rho_0 R^2 = 1.2$. The top panel shows the radial distribution function $g(r)$, the middle panel the static structure factor $S(k)$, and bottom panel the dispersion relation $\omega(k)$.

is one main peak in $\omega(k)$, with its maximum close to zero, indicating that this state point is close to but slightly outside the linear instability threshold. As a increases this peak grows in height and also shifts to slightly larger wave numbers, as the uniform liquid becomes linearly unstable. At the same time a second peak starts to develop at $kR \approx 3$ and becomes
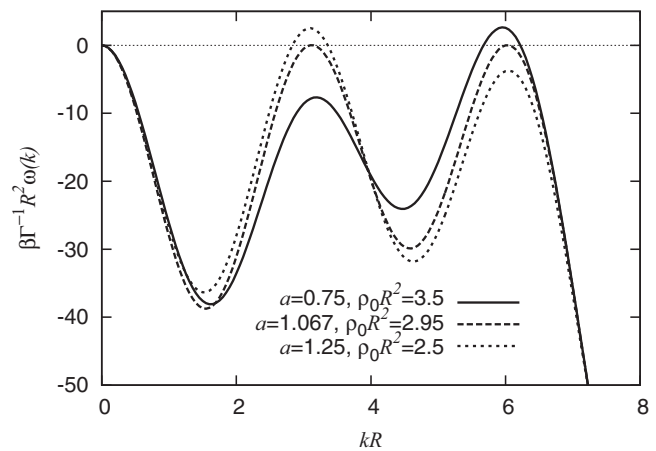

FIG. 6. Dispersion relation $\omega(k)$ at a series of points along a diagonal path in the phase diagram passing through the point at $\rho_0 R^2 = 2.95$ and $a = 1.067$ at which the two modes $k_1 R = 3.12$ and $k_2 R = 6.03$ are simultaneously marginally unstable. Note that $k_2/k_1 = 1.932$.
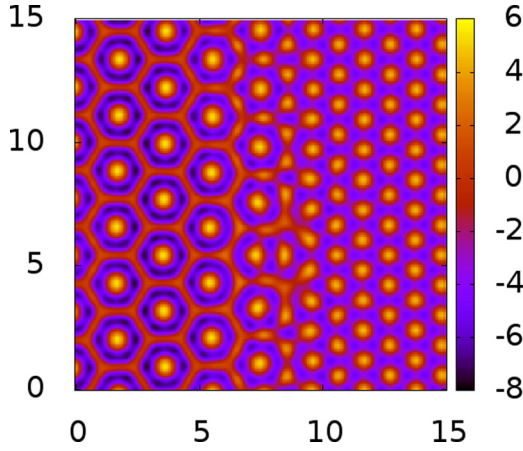
FIG. 7. (Color online) Density profile in the top panel of Fig. 2 displayed in terms of the logarithm of the density $\ln[\rho(\mathbf{r})R^2]$ plotted in the $(x/R, y/R)$ plane. This representation allows one to see the fine structure of the density profile away from the principal peaks. Note in particular the honeycomb structure surrounding each of the peaks in the crystal A phase on the left of the interface.
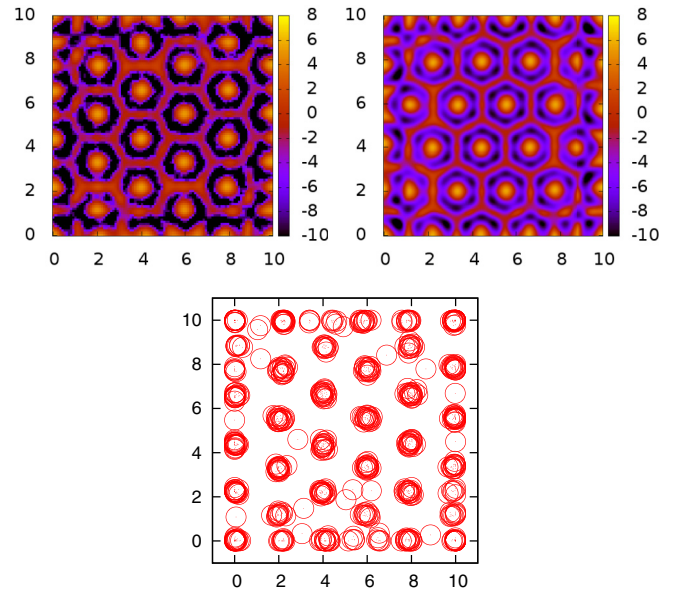

FIG. 8. (Color online) The top panels show $\ln[\rho(\mathbf{r})R^2]$ in the $(x/R, y/R)$ plane for a system of $N = 600$ particles with $(a, \rho_0 R^2) = (0.8, 6)$ confined in a square region of side $L = 10R$ obtained from BD simulations (top left) and DFT (top right). The system forms crystal A with a density profile consisting of an array of peaks surrounded by a connected network within which the particles are free to move; this is the crystal-liquid state. The bottom panel is a snapshot from the BD simulation where each particle coordinate is plotted as an open circle.

inspection of the density profile of the crystal A phase reveals that this is not the case, at least at state points near its coexistence with the crystal B phase (i.e., at smaller a values). In Fig. 7 we display the density profile in the vicinity of the interface between the crystal A and crystal B phases shown in Fig. 2, but this time in terms of the logarithm of the density $\ln[\rho(\mathbf{r})R^2]$. This allows one to see the fine structure in the density profile in the regions of space between the main peaks of the hexagonal lattice. Here we see an unbroken honeycomblike network of density that percolates throughout the crystal A portion of the system, indicating that the particles that contribute to this portion of the density profile are free to move throughout the system. To confirm the existence of this striking structure, we calculate, using both DFT and BD computer simulations, the density profile for a system confined within a square confining potential $\Phi(\mathbf{r})$ with hard walls at $x = 0, 10R$ and $y = 0, 10R$ so that $\Phi(x, y) = 0$ for $(0,0) < (x, y) < (10R, 10R)$ and $\Phi(x, y) = \infty$ otherwise. The top left panel in Fig. 8 shows the density profile obtained from the BD simulations with $N = 600$ particles, $\beta\epsilon = 1$, and $a = 0.8$, i.e., the average density in the box is $\rho_0 R^2 = 6$. The BD result is obtained simply by evolving in time the particles according to Eq. (14) and then averaging over their positions to calculate the density profile. The top right panel in Fig. 8 shows the corresponding density profile from DFT. The remarkable agreement between the two confirms the validity of the DFT approximation for this system. The bottom panel in Fig. 8 shows a snapshot showing a typical configuration of the particles in the BD simulation. The particle positions are indicated using open circles. Although the majority of the particles is located on lattice sites, a significant minority remains mobile, with the particles free to move in the density lanes between lattice sites. The system thus consists of two dynamically distinct populations. This is not observed in other pattern-forming 2D systems, such as those in Refs. [56–59], where the dynamics of all the particles are identical.

In Fig. 9, bottom panel, we display the percentage of mobile particles in crystal A as a function of the parameter a, for a fixed value of the chemical potential $\beta\mu = 39$. This percentage is obtained by integration over all portions of the density profile that are a distance $0.65R$ away from the center of the density peaks. Particles that contribute to this portion of the density are defined to be mobile. Figures 9(a)–9(d) display the logarithm of the density profile corresponding to the points indicated in the lower panel. We see that as a decreases the fraction of mobile particles increases from zero, reaching a value of over 7% at $a = 0.75$. We terminate the curve at this point because for $a < 0.75$ crystal A is no longer the equilibrium crystal structure. It appears that as a decreases below this coexistence value, the growing proportion of mobile particles triggers the formation of the smaller lattice spacing crystal B phase, whereby the mobile particles freeze to form the additional peaks of crystal B.

V. FORMATION OF QUASICRYSTALS

The role of resonant triads in the context of minimizing a free energy with one length scale has long been recognized [60,61]. In particular in three dimensions these triads can stabilize states with icosahedral symmetry. In two dimensions the presence of two length scales implies the presence of two circles of wave vectors in Fourier space and resonant triads involving wave vectors from these two circles can also contribute to stability of quasicrystals [26], provided the interaction coefficients are of the correct sign. With a radius ratio of the two circles equal to $2\cos(15°) = 1.932$,
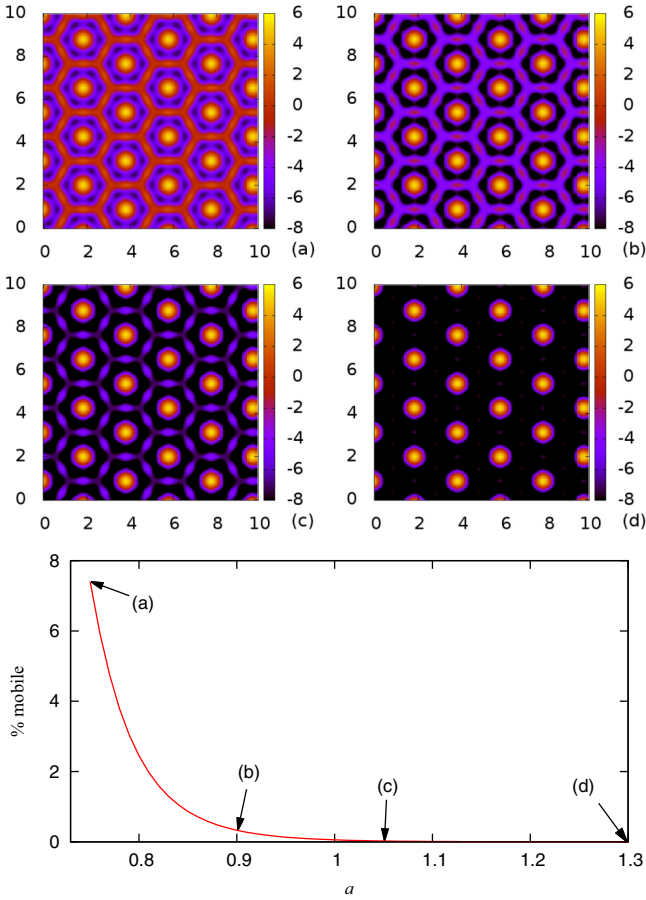
FIG. 9. (Color online) (a)–(d) Plots of $\ln[\rho(\mathbf{r})R^2]$ in the crystal A phase in the $(x/R, y/R)$ plane for fixed $\beta\mu = 39$ at the state points: (a) $(a, \rho_0 R^2) = (0.75, 4.1)$, (b) $(0.9, 3.8)$, (c) $(1.05, 3.5)$, and (d) $(1.3, 3.1)$. The bottom figure shows a plot of the fraction of mobile particles that are in the liquid part of the density surrounding the density peaks. For $a < 0.75$ crystal A is no longer the thermodynamic equilibrium crystal structure and is replaced by crystal B.

equilateral triads, $30°$ triads and $150°$ triads involving two vectors from one circle and one vector from the other, increase the number of possible triads and so the potential contribution to the free energy. This configuration leads to dodecagonal quasicrystals; with other radius ratios, the situation can be yet more complicated [25]. In fact, arguments based on the contribution to the free energy from resonant triads only, important though these are, overlook the potential importance of higher-order harmonics, whose coefficients may become arbitrarily large owing to the problem of small divisors that inevitably appears whenever quasiperiodicity and nonlinearity occur together [62]. Thus a truncation of the theory at cubic order, a procedure widely used in the literature, remains to be properly justified, although Ref. [63] goes some way towards resolving the small divisor issue.

The mechanism identified below for stabilizing QCs in the present system also involves two length scales, but differs qualitatively from that just described (see also [28,29]). In our case the system first forms the small length scale crystal phase. It is only when this phase is almost fully formed (i.e., when the dynamics is far into the nonlinear regime) that the longer

length scale starts to appear, leading to the formation of the QC (see Figs. 10 and 11). Thus, what we observe is in fact a hitherto unseen mechanism for the formation of QCs.

The scenario for the formation of QCs described in [28] (i) requires the system to be *just* inside the linear instability line (i.e., ρ is restricted to a small range beyond ρ_λ, the value at the linear instability line) and (ii) relies on the simultaneous *linear growth* of two distinct wave numbers as in [26]. In this scenario the role of the higher-order interactions (i.e., of nonlinearity) is to stabilize the two length scale (QC) structures formed from the two linearly growing scales [28].

We contrast this scenario with that described here for a uniform liquid quenched to a region above the coexistence of the two crystal phases but below the pink dotted line in Fig. 1. In this regime the large k peak dominates and small length scale density fluctuations grow rapidly (Fig. 10) as described by the dispersion relation in Fig. 12(a). In this regime the system behaves as if it were going to form crystal B. However, the true minimum of the free energy corresponds to the larger length scale crystal and this length scale is linearly *stable* [Fig. 12(a)]. As a result, as the growing short-scale density fluctuations reach the nonlinear regime, the system seeks to go to the longer length scale structure but the smaller length scale imprinted from the linear growth regime leads to frustration. We observe this type of behavior well away from onset, i.e., deep inside the linear instability threshold, in contrast to the scenario in [28]. In Fig. 10 we display the resulting time evolution of the density profile as the system forms QCs. Since only one mode is unstable, the formation of the QCs that we find can only occur via the nonlinear mechanism described here.

In Fig. 11 we display DDFT results showing the formation of a QC structure at $a = 1.067$ and $\rho_0 R^2 = 3.5$.[2] The dispersion relation corresponding to this state point is shown in Fig. 12(b). We see that in this case the larger-wavelength mode is no longer stable, although its growth rate is weak compared to that of the short-wavelength mode. As a result, the system first forms the pure small length scale crystal (see, e.g., the middle panel of the top row of Fig. 11 corresponding to $t^* = t/\tau_B = 2$, where $\tau_B \equiv \beta R^2/\Gamma$ is the Brownian time scale). However, over time, starting from a grain boundary, the system evolves a QC structure much as occurs at state point $a = 0.8$ and $\rho_0 R^2 = 3.5$. In both cases this happens when the system is well away from the linear regime, in contrast to the weakly nonlinear QC mechanism proposed in Refs. [28,29]. Indeed, for $a = 1.067$ the linear instability line is at $\rho_0 R^2 = 2.95$, implying that this state point corresponds, like $a = 0.8$ and $\rho_0 R^2 = 3.5$, to quite a deep quench. As a result, both snapshot series show that the linear growth regime introduces only *one* length scale, that of the small length scale crystal B phase, despite the presence of the weakly unstable larger length scale in Fig. 11. Figure 11 also confirms that the DDFT dynamics and the fictitious dynamics obtained from Picard iteration in Fig. 10 are indeed qualitatively very similar.

As explained above, our work shows that quasicrystalline structures can form even when only one of the two scales introduced by our choice of the potential is unstable; the instability forms nonlinear structures with this one scale only

---

[2]Figure 2 of Ref. [6] displays a QC formed at $(a, \rho_0 R^2) = (0.76, 3.5)$.
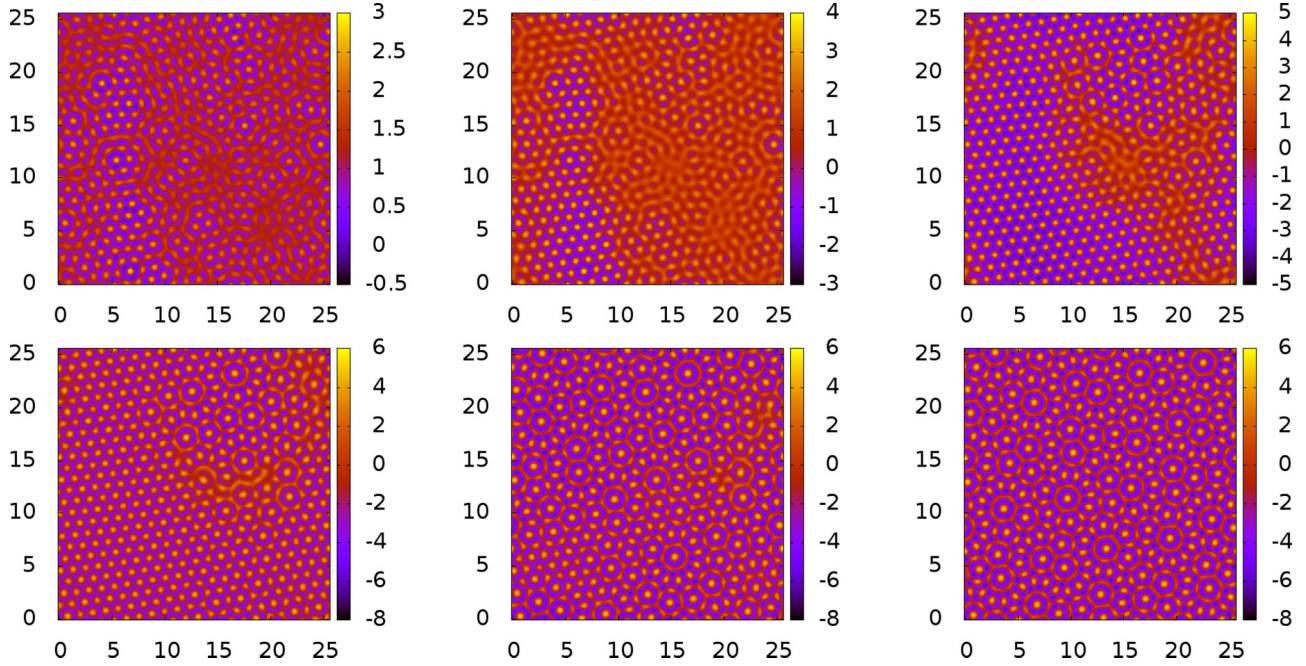
FIG. 10. (Color online) Snapshots of $\ln[\rho(\mathbf{r})R^2]$ in the $(x/R, y/R)$ plane obtained via Picard iteration for $a = 0.8$ and $\rho_0 R^2 = 3.5$, revealing the evolution towards the equilibrium state for the same state point as the results displayed in the upper panel of Fig. 13. The dispersion relation at this state point is displayed in Fig. 12(a). The panels along the top row, from left to right, correspond to times $t = 30$, 32, and 35 and along the bottom row to $t = 40$, 50, and 200. Note that the system first forms the small length scale crystal (at time $t \approx 30$). It then tries to form the longer length scale crystal. However, due to the small length scale already imprinted on the system, it cannot form a perfect large length scale crystal and ends up forming a disordered system with domains of QC ordering. The Picard iteration used to generate these figures does not locally conserve particle number (although it does conserve the total density in the system; see Sec. II), but is much faster than the full DDFT and gives qualitatively similar results; compare this figure with Fig. 11, which is calculated with DDFT.
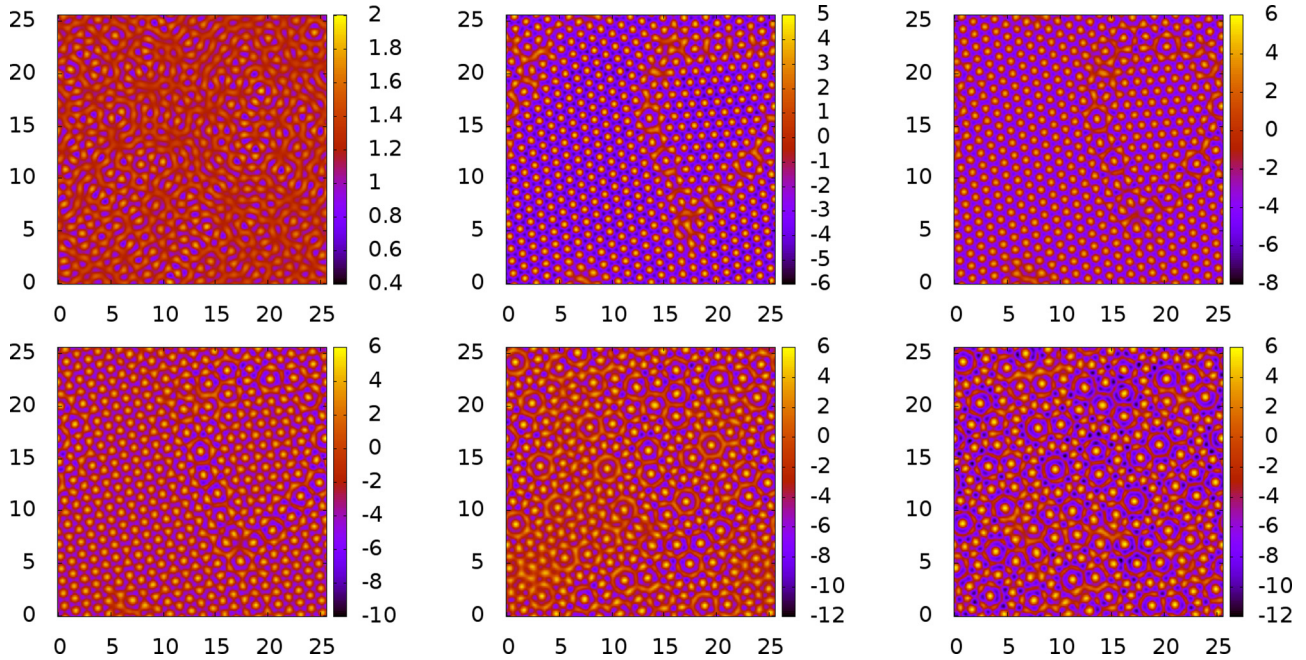

FIG. 11. (Color online) Snapshots of $\ln[\rho(\mathbf{r})R^2]$ in the $(x/R, y/R)$ plane obtained from DDFT, for $a = 1.067$ and $\rho_0 R^2 = 3.5$. The dispersion relation at this state point is displayed in Fig. 12(b). The panels along the top row, from left to right, correspond to times $t/\tau_B \equiv t^* = 1$, 2, and 5 and along the bottom row to $t^* = 10$, 20, and 40, where $\tau_B \equiv \beta R^2/\Gamma$ is the Brownian time scale. Note that the system first forms a small length scale crystal ($t^* = 2$). It then tries to form the longer length scale crystal, initiated from a grain boundary; see panels for $t^* = 5$ and 10. However, because of the small length scale already imprinted on it, the system cannot form a perfect long length scale crystal and ends up forming a disordered system with domains of QC ordering; see the final stationary profile at $t^* = 40$.
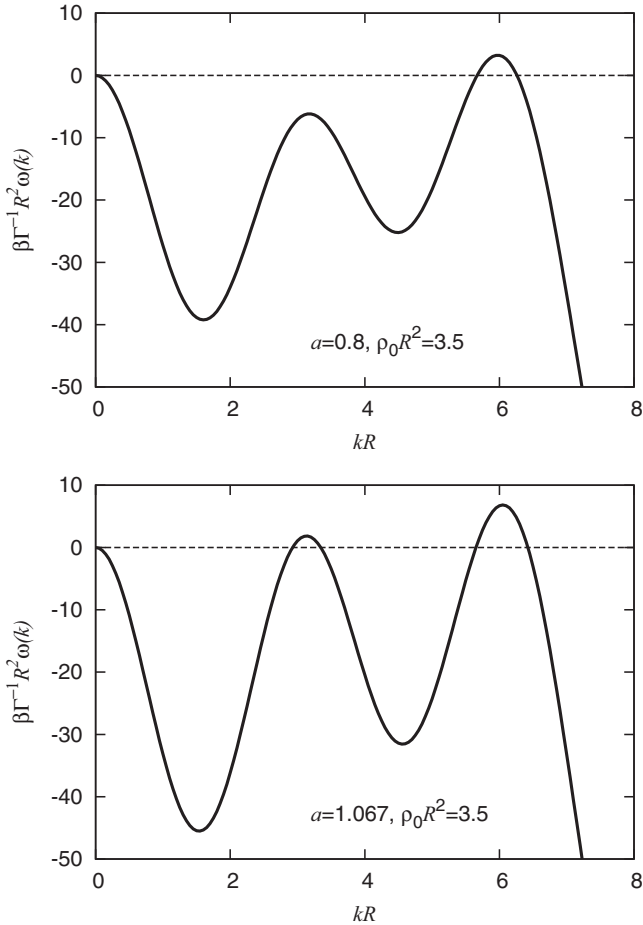
FIG. 12. Dispersion relation at the state point $a = 0.8$ and $\rho_0 R^2 = 3.5$ (top, corresponding to Fig. 10) and $a = 1.067$ and $\rho_0 R^2 = 3.5$ (bottom, corresponding to Fig. 11). In both cases, QCs form at these state points. In the upper panel (Fig. 10) only one mode is unstable, corresponding to the smaller length scale crystal B. In the lower panel (Fig. 11) two modes are unstable, but the growth rate for the smaller length scale crystal B is much larger than that for the larger length scale crystal A.

but because these do not correspond to the global minimum of the free energy that occurs at a distinct scale, the system attempts to shift the structure to the thermodynamically preferred scale. This process leads to frustration that is responsible for the formation of the QC state. This is a qualitatively distinct mechanism of QC formation from that advocated in Refs. [28,29], which requires that both scales are weakly unstable. As a result, the latter theory is only capable of describing QCs that have very small amplitude. In contrast, our quasicrystalline states are present quite far from the onset of instability and form from a periodic state via the nonlinear time-dependent process described above.

The calculation of the values of a and R_s/R used above to home in on the parameter region where QCs might be observed was described in Ref. [28] as well as in earlier work [18]. Once the approximate parameter regime has been identified, the details of what happens depend on the values of a and R_s/R. However, the QCs that we observe are always *metastable* with respect to the periodic crystal. By this we mean that they
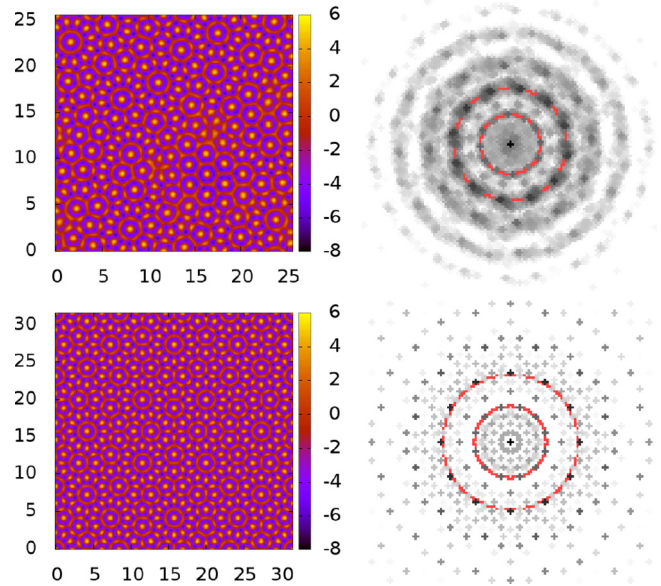

FIG. 13. (Color online) The left panels show plots of $\ln[\rho(\mathbf{r})R^2]$ in the $(x/R, y/R)$ plane obtained from DFT for $(a, \rho_0 R^2) = (0.8, 3.5)$. The right panels are the corresponding Fourier transforms. The latter exhibit 12-fold symmetry, which is indicative of QC ordering. The top density profile is obtained from random initial conditions, while the lower profile was formed starting from an initial density profile having QC symmetry.

correspond to a local minimum of the free energy, but not to the global minimum (Fig. 14). Thus the density profiles in Fig. 13 are indeed possible ground states (i.e., local minima), but not *the* ground state (global minimum): the free energy of the state in the top panel in Fig. 13 is slightly higher than that of the lower panel, but both are higher than that of the crystal A phase, which is the global minimum for this state point. As a increases beyond the range displayed in Fig. 14, the QC free energy increases more rapidly than that of the crystal A phase, i.e., the trend revealed in Fig. 14 continues and the two free energies do not approach one another again. In particular, the QC free energy is far above that of the crystal A phase at $a = 1.067$. This may also be so for the QCs obtained in Refs. [28,64,65]. In contrast, very recently [66] it has been
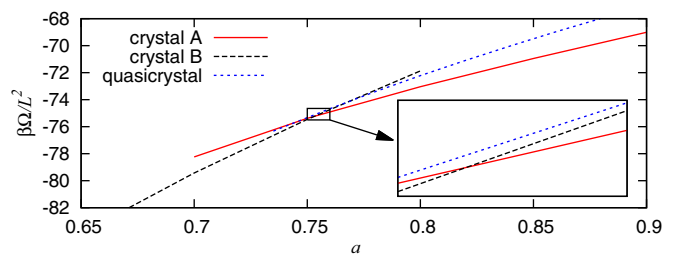

FIG. 14. (Color online) Grand potential density as a function of a for fixed $\beta\mu = 39$ for the two different crystal structures and also the QC solution displayed in Fig. 13. Near $a = 0.75$ there is a point where all three have almost the same value of the grand potential, but the QC solution is never the global minimum (see the inset). The crystal A phase is of crystal-liquid type throughout the range of a shown.
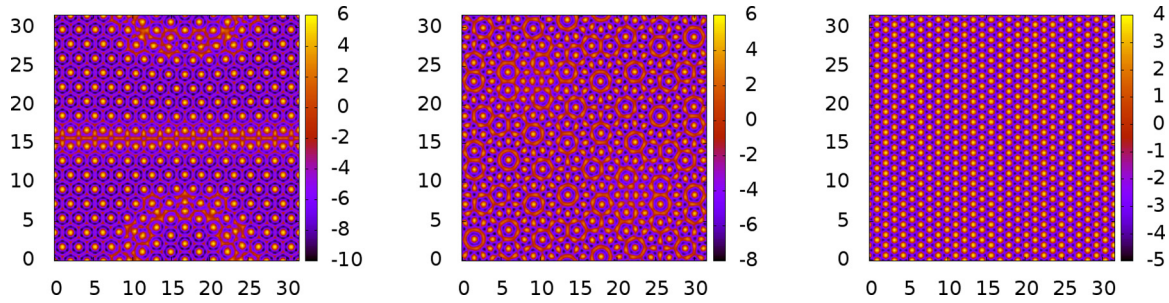
FIG. 15. (Color online) Plots of $\ln[\rho(\mathbf{r})R^2]$ in the $(x/R,y/R)$ plane for density profiles obtained when starting from the perfect QC displayed on the bottom left of Fig. 13, which has $R_s/R = 1.855$, and then following the solution as R_s is varied, for fixed μ and domain size. When R_s is decreased, the QC remains stable until $R_s/R = 1.77$, at which point the QC profile becomes linearly unstable and the Picard iteration then falls on to the crystal A profile (which contains defects), displayed above left. When R_s is instead increased, the perfect QC solutions become unstable at $R_s/R = 2.03$, where the iteration switches to a different branch of QC solutions (above middle), before this new QC state becomes unstable at $R_s/R = 2.19$ and evolves to the crystal B branch of solutions displayed above right.

shown that for the Lifshitz-Petrich free energy [26], QCs are indeed the global free energy minimum for certain parameter values.

In Fig. 13 we display both the QC density profiles and the corresponding Fourier transforms. Both exhibit 12-fold ordering. In the upper case, there is significant disorder in the system, which is not surprising given the dynamical mechanism we observe for QC formation. However, it is possible to facilitate a more ordered final state by choosing (for example) a periodic domain 30 times larger than the shorter of the two length scales to allow for a circle of 12 vectors that are $29.98°$ apart and whose lengths differ by 0.05% [17]. Starting from an initial condition with these 12 modes set to a small amplitude, we observe that the system easily forms a perfect example of a QC (Fig. 13, lower panels).

In Fig. 15 we display density profiles obtained by taking this perfect QC and then following the solution as the value of R_s is changed. We find that QCs remain linearly stable in the Picard iteration for $1.77 < R_s/R < 2.18$. If R_s is decreased to $R_s/R = 1.77$, the QC solution at this point becomes unstable and the Picard iteration leaves this solution and falls onto a crystal A profile (which contains defects), displayed in the left-hand panel of Fig. 15. If instead R_s is increased, at $R_s/R = 2.03$ the Picard iteration falls off the branch of solutions corresponding to the perfect QC at the bottom left of Fig. 13 and settles on a different branch of QC solutions, which is displayed in the middle panel of Fig. 15. Further increasing R_s, this QC becomes linearly unstable at $R_s/R = 2.18$ and the Picard iteration then goes to the crystal B profile displayed in the right-hand panel of Fig. 15.

VI. CONCLUSION

In this paper we have elaborated on the results of Ref. [6] for a simple model soft-core fluid that exhibits surprisingly rich phase behavior: two crystalline phases and a fluid phase. This stems from the fact that the pair potential between the particles has two length scales R and R_s and two different energy scales $a\epsilon$ and $(1 + a)\epsilon$. The subtle balance of these leads to rich structuring and phase behavior. Pair potentials with these qualities arise as the effective interaction potentials between polymeric macromolecules. In particular, we believe

that tailoring dendrimers with a core plus shell architecture should yield particles with effective interaction potentials akin to those considered here. Of course, the model system considered here is two dimensional, so to observe the particular behavior reported here in an experimental system, the particles must be confined to an interface in order to create an effectively two-dimensional system. The natural next step to take after the work described here is to consider systems in three dimensions, where the phase behavior and the structures observed will be even richer.

The two most striking aspects of the present model are (i) the formation of the crystal-liquid phase, having two dynamically distinct populations of particles, some that are confined to the crystal lattice sites and others that are mobile, residing in a honeycomblike network around the main density peaks, and (ii) the formation of QCs. This aspect is particularly interesting because the QC structures form via a mechanism that is distinct from any of the mechanisms that have been proposed previously. Namely, QC formation occurs following a deep quench of the uniform liquid to state points where it is unstable. At these state points, the global minimum of the free energy corresponds to the large length scale crystal A phase. However, in the initial linear growth regime after the quench, a smaller length scale (corresponding to the small-length crystal B phase) grows the fastest, leading to the system becoming patterned with the wrong small-wavelength density modulations. When the system subsequently seeks to lower its free energy and hence to introduce the longer length scale, it remains stuck with some ordering on the small length scale. The final equilibrium structure generally consists of a mixture of the two length scales and may exhibit QC ordering, i.e., the Fourier transform may consist of a ring of 12 peaks. The resulting structure is in fact a local minimum of the free energy, but not the global minimum. The QCs formed via such a mechanism are, unsurprisingly, generally disordered, containing a mixture of domains with 12-fold ordering and domains of hexagonal ordering, corresponding to one of the two hexagonal crystal structures.

The results presented here are for just one temperature. However, the important quantities for determining the phase behavior of the model are the dimensionless quantities $k_B T/\epsilon$, a, and R_s/R. Varying these determines the location in the phase

diagram of the linear instability threshold, the point where both length scales are marginally unstable, and the ratio k_2/k_1. In the limit $a = 0$, increasing $k_B T/\epsilon$ shifts the linear instability threshold to higher density ρ [54]. Varying the temperature by a modest amount should leave the behavior of the present system qualitatively unchanged, merely shifting the regions where the crystalline phases occur to higher densities.

It is worth connecting the present work with related work [54,67,68] on the freezing of binary mixtures of particles. The mixtures considered in Refs. [54,67] also possess two length scales, owing to the fact that they are a binary mixture of soft particles of different sizes, and form multiple structures when a solidification front advances into an unstable uniform liquid. For a deep enough quench, such a front deposits behind it density modulations that are also of the wrong wavelength, thereby frustrating the formation of a well-ordered correct wavelength equilibrium crystal. In particular, the final equilibrium structures also contain a high degree of disorder. In this case, the selection of the wrong wavelength is due to the dynamical nature of the length scale selection process via an advancing front: the selected wavelength depends only on the linearization (17), whereas the global minimum free energy crystal structure is determined by the full DFT, which is highly nonlinear. This situation differs from the QC formation observed in the present work, yet there are similarities: both systems undergo a linear process that generates modulations with a length scale that does not correspond to the length scale of the equilibrium structure, which is determined by nonlinear processes. This naturally leads to an unanswered question: what happens when a solidification front advances in the present system? The front motion will generate a particular length scale, the linear growth of local density modulations will produce a slightly different length scale, and nonlinear interactions will seek to generate a third length scale. We anticipate that the interplay of such processes will inevitably lead to highly disordered structures.

ACKNOWLEDGMENTS

[1] C. N. Likos, Phys. Rep. **348**, 267 (2001).

[2] C. N. Likos, H. Löwen, M. Watzlawek, B. Abbas, O. Jucknischke, J. Allgaier, and D. Richter, Phys. Rev. Lett. **80**, 4450 (1998).

[3] C. N. Likos and H. M. Harreis, Condens. Matter Phys. **5**, 173 (2002).

[4] B. M. Mladek, G. Kahl, and C. N. Likos, Phys. Rev. Lett. **100**, 028301 (2008).

[5] D. A. Lenz, R. Blaak, C. N. Likos, and B. M. Mladek, Phys. Rev. Lett. **109**, 228301 (2012).

[6] A. J. Archer, A. M. Rucklidge, and E. Knobloch, Phys. Rev. Lett. **111**, 165501 (2013).

[7] B. M. Mladek, D. Gottwald, G. Kahl, M. Neumann, and C. N. Likos, Phys. Rev. Lett. **96**, 045701 (2006).

[8] C. N. Likos, B. M. Mladek, D. Gottwald, and G. Kahl, J. Chem. Phys. **126**, 224502 (2007).

[9] B. M. Mladek, D. Gottwald, G. Kahl, M. Neumann, and C. N. Likos, J. Phys. Chem. B **111**, 12799 (2007).

[10] C. N. Likos, B. M. Mladek, A. J. Moreno, D. Gottwald, and G. Kahl, Comput. Phys. Commun. **179**, 71 (2008).

[11] B. M. Mladek, P. Charbonneau, C. N. Likos, D. Frenkel, and G. Kahl, J. Phys.: Condens. Matter **20**, 494245 (2008).

[12] K. Zhang, P. Charbonneau, and B. M. Mladek, Phys. Rev. Lett. **105**, 245701 (2010).

[13] N. B. Wilding and P. Sollich, J. Chem. Phys. **141**, 094903 (2014).

[14] A. J. Moreno and C. N. Likos, Phys. Rev. Lett. **99**, 107801 (2007).

[15] B. Christiansen, P. Alstrom, and M. T. Levinsen, Phys. Rev. Lett. **68**, 2157 (1992).

[16] W. S. Edwards and S. Fauve, Phys. Rev. E **47**, R788 (1993).

[17] A. M. Rucklidge and M. Silber, SIAM J. Appl. Dyn. Syst. **8**, 298 (2009).

[18] H. W. Müller, Phys. Rev. E **49**, 1273 (1994).

[19] B. Christiansen, P. Alstrom, and M. T. Levinsen, J. Fluid Mech. **291**, 323 (1995).

[20] W. B. Zhang and J. Viñals, J. Fluid Mech. **336**, 301 (1997).

[21] A. Kudrolli, B. Pier, and J. P. Gollub, Physica D **123**, 99 (1998).

[22] H. Arbell and J. Fineberg, Phys. Rev. E **65**, 036224 (2002).

[23] Y. Ding and P. Umbanhowar, Phys. Rev. E **73**, 046305 (2006).

[24] C. M. Topaz, J. Porter, and M. Silber, Phys. Rev. E **70**, 066206 (2004).

[25] A. M. Rucklidge, M. Silber, and A. C. Skeldon, Phys. Rev. Lett. **108**, 074504 (2012).

[26] R. Lifshitz and D. M. Petrich, Phys. Rev. Lett. **79**, 1261 (1997).

[27] A. C. Skeldon and A. M. Rucklidge, J. Fluid Mech. **777**, 604 (2015).

[28] K. Barkan, H. Diamant, and R. Lifshitz, Phys. Rev. B **83**, 172201 (2011).

[29] K. Barkan, M. Engel, and R. Lifshitz, Phys. Rev. Lett. **113**, 098304 (2014).

[30] S. Lee, M. J. Bluemle, and F. S. Bates, Science **330**, 349 (2010).

[31] S. Fischer, A. Exner, K. Zielske, J. Perlich, S. Deloudi, W. Steurer, P. Lindner, and S. Forster, Proc. Natl. Acad. Sci. USA **108**, 1810 (2011).

[32] C. R. Iacovella, A. S. Keys, and S. C. Glotzer, Proc. Natl. Acad. Sci. USA **108**, 20935 (2011).

[33] C. H. Xiao, N. Fujita, K. Miyasaka, Y. Sakamoto, and O. Terasaki, Nature (London) **487**, 349 (2012).

[34] M. Engel, P. F. Damasceno, C. L. Phillips, and S. C. Glotzer, Nat. Mater. **14**, 109 (2015).

[35] C. Jin, B. Cheng, B. Man, Z. Li, D. Zhang, S. Ban, and B. Sun, Appl. Phys. Lett. **75**, 1848 (1999).

[36] M. E. Zoorob, M. D. B. Charlton, G. J. Parker, J. J. Baumberg, and M. C. Netti, Nature (London) **404**, 740 (2000).

[37] E. Macia, Rep. Prog. Phys. **75**, 036502 (2012).

[38] M. Dzugutov, Phys. Rev. Lett. **70**, 2924 (1993).

[39] A. R. Denton and H. Löwen, Phys. Rev. Lett. **81**, 469 (1998).

[40] J. Roth and A. R. Denton, Phys. Rev. E **61**, 6845 (2000).

[41] A. S. Keys and S. C. Glotzer, Phys. Rev. Lett. **99**, 235503 (2007).

[42] T. Dotera, T. Oshiro, and P. Ziherl, Nature (London) **506**, 208 (2014).

[43] R. Evans, Adv. Phys. **28**, 143 (1979).

[44] R. Evans, *Fundamentals of Inhomogeneous Fluids* (Dekker, New York, 1992).

[45] J. F. Lutsko, Adv. Chem. Phys. **144**, 1 (2010).

[46] J.-P. Hansen and I. R. McDonald, *Theory of Simple Liquids*, 2nd ed. (Academic, London, 1986).

[47] U. Marini, B. Marconi, and P. Tarazona, J. Chem. Phys. **110**, 8032 (1999).

[48] U. Marini, B. Marconi, and P. Tarazona, J. Phys.: Condens. Matter **12**, A413 (2000).

[49] A. J. Archer and R. Evans, J. Chem. Phys. **121**, 4246 (2004).

[50] A. J. Archer and M. Rauscher, J. Phys. A: Math. Gen. **37**, 9325 (2004).

[51] A. Lang, C. N. Likos, M. Watzlawek, and H. Löwen, J. Phys.: Condens. Matter **12**, 5087 (2000).

[52] A. A. Louis, P. G. Bolhuis, and J.-P. Hansen, Phys. Rev. E **62**, 7961 (2000).

[53] R. Roth, J. Phys.: Condens. Matter **22**, 063102 (2010).

[54] A. J. Archer, M. C. Walters, U. Thiele, and E. Knobloch, Phys. Rev. E **90**, 042404 (2014).

[55] A. J. Archer, M. J. Robbins, U. Thiele, and E. Knobloch, Phys. Rev. E **86**, 031603 (2012).

[56] M. A. Glaser, G. M. Grason, R. D. Kamien, A. Kosmrlj, C. D. Santangelo, and P. Ziherl, Europhys. Lett. **78**, 46004 (2007).

[57] A. Imperio and L. Reatto, J. Phys.: Condens. Matter **16**, S3769 (2004).

[58] A. Imperio and L. Reatto, J. Chem. Phys. **124**, 164712 (2006).

[59] A. J. Archer, Phys. Rev. E **78**, 031402 (2008).

[60] S. Alexander and J. McTague, Phys. Rev. Lett. **41**, 702 (1978).

[61] P. Bak, Phys. Rev. Lett. **54**, 1517 (1985).

[62] A. M. Rucklidge and W. J. Rucklidge, Physica D **178**, 62 (2003).

[63] G. Iooss and A. M. Rucklidge, J. Nonlinear Sci. **20**, 361 (2010).

[64] C. V. Achim, M. Schmiedeberg, and H. Löwen, Phys. Rev. Lett. **112**, 255501 (2014).

[65] J. Rottler, M. Greenwood, and B. Ziebarth, J. Phys.: Condens. Matter **24**, 135002 (2012).

[66] K. Jiang, J. Tong, P. Zhang, and A.-C. Shi, arXiv:1505.07300.

[67] A. J. Archer, M. C. Walters, U. Thiele, and E. Knobloch, arXiv:1505.07976.

[68] F. Scheffler, P. Maass, J. Roth, and H. Stark, Eur. Phys. J. B **42**, 85 (2004).